J Biomed Eng Syst Technol Low Middle Income Ctries 2026; 1(1): 57 –75

Journal of Biomedical Engineering Systems and Technologies for Low- and Middle-Income Countries

Curcumin-loaded Dual Coated Chitosan-Silica Magnetite Nanoparticles for Targeted Drug Delivery: A Novel Approach for Improving Health Outcomes In Low- and Middle-Income Countries

Nyarko JA[1 *], Gati J [1], Agbe H[1], Adjei PE[2], Antwi-Baah R[3]

[1] Department of Materials and Metallurgical Engineering, College of Engineering, Kwame Nkrumah University of Science and Technology, Kumasi, Ghana
[2] Department of Biomedical Engineering, College of Engineering, Kwame Nkrumah University of Science and Technology, Kumasi, Ghana
[3] College of Ecology and Environment, Chengdu University of Technology, Chengdu, 610059, China

*Corresponding author: Joshua Amuzu Nyarko (janyarko9@st.knust.edu.gh)

Abstract

Targeted drug delivery systems can enhance treatment efficacy while reducing the adverse effects associated with conventional drug delivery. Many traditional methods suffer from poor bioavailability, rapid degradation, and limited targeting efficiency. We report the synthesis, characterization, and application of curcumin-loaded silica- and chitosan-coated magnetite nanoparticles as a low-cost drug delivery system. Both coated and uncoated nanoparticles were compared to evaluate drug release performance. Magnetite nanoparticles were synthesized using maize leaf extract, while chitosan was derived from crab shells via demineralization, deproteination, and deacetylation. Silica coating was applied using a sol-gel process to enhance nanoparticle stability and drug retention. The resulting dual-coated chitosan-silica-magnetite composites were characterized using Fourier Transform Infrared Spectroscopy (FTIR), Scanning Electron Microscopy (SEM), Energy Dispersive Spectroscopy (EDS), and X-Ray Diffraction (XRD). Drug loading and release studies were conducted to determine entrapment efficiency and release kinetics. The findings demonstrate that the 75 wt% formulation achieved the highest entrapment efficiency, with sustained drug release over

s. This dual-coating system offers a promising strategy for curcumin delivery and could be adapted to support affordable cancer therapy, particularly in low- and middle-income countries

Keywords; *Chitosan, Magnetite, Nanoparticles, Drug Delivery, Targeted Therapy,Curcumin, LMICs.*

editor@best-lmic.org, www.best-lmic.org Post Office Box 00800-13975, Westlands, Nairobi, Kenya.

1.0 Introduction

Cancer is the second leading cause of death worldwide, with approximately 10 million deaths recorded in 2020.[1] Notably, 70% of these deaths occurred in low- and middle-income countries (LMICs) due to limited access to early diagnosis and advanced treatments.[2] The disparity is even more striking in cervical cancer, where 90% of new cases and deaths occur in LMICs, despite being treatable if diagonised early through early screening.[3] Cancer cases in sub-Saharan Africa are projected to increase by more than 92% between 2020 and 2040, further straining already fragile healthcare systems.[1]

Despite significant advancements in drug delivery systems, LMICs face challenges such as inadequate healthcare infrastructure, high treatment costs, and limited access to precision medicine, exacerbating the impact of cancer. Conventional drug administration methods, including oral and intravenous chemotherapy, are plagued by severe systemic toxicity, poor bioavailability, and non-specific drug distribution.[4,5] These limitations necessitate the development of cost-effective, targeted drug delivery systems that enhance therapeutic efficiency while minimizing side effects.[6]

Recent advances in Nanotechnology-based drug delivery systems have been able to address these limitations by enabling controlled drug release, improving bioavailability, and targeted therapy.[7] Among these platforms, magnetite nanoparticles coated with both silica and chitosan have emerged as a promising strategy.[8] Silica provides thermal and structural stability to the magnetite core, while chitosan enhances biocompatibility, drug encapsulation, and pH-responsive release.[8, 9]

This dual-coating approach has been shown to outperform single-layer systems in terms of drug retention, release control, and magnetic responsiveness.[9] Chitosan is a sugar that is obtained from the hard outer skeleton of shellfish, including crabs and shrimps.[10] Crabs are mostly important sources of minerals and nutrients to humans, but their shells are mostly disposed of incorrectly, polluting the marine environment.[11] However, these disposed shells could be processed into chitosan for beneficial purposes.

Moreover, in this study, an eco-friendly approach, using maize leaf extract, is used to synthesize magnetite nanoparticles. Due to the lower cost of production and minimal usage of toxic solvents, plant-based green synthesis has been shown to lower costs and reduce chemical waste by avoiding the use of toxic solvents.[12,13] The minute nature of these nanoparticles enables effective delivery of drugs to target tissues. Their tiny size enables passing through biological barriers to delivering drugs to targeted tissues in the body.[14]

In this targeted drug delivery strategy, the curcumin drug is coupled to magnetic nanoparticles that can be directed to the affected cells using external magnetic fields.[15] When the nanoparticles reach their target, the drugs are released under the influence of an alternating magnetic field. The release of drugs loaded on magnetite nanoparticles may be maintained over a longer period by adopting a silica-based coating strategy, as silica provides structural integrity and enhances sustained release. Silica provides better stability to magnetite nanoparticles.[16]

While prior studies have employed either silica or chitosan as standalone coatings, there is a notable gap in combining both materials to achieve their synergistic benefits.[17, 18] This study addresses that gap by synthesizing and evaluating chitosan-coated silica-magnetite nanoparticles for curcumin delivery, with an emphasis on cost-effective cancer therapy suited for LMICs.

In the study, Chitin was initially extracted through demineralization and deproteination processes to obtain a purer form, yielding a fine powder with particle size reduced to approximately 150 µm through grinding and sieving. The extracted chitin then underwent deacetylation to form chitosan[19], a crucial step in enhancing its biocompatibility and drug-loading capacity. Magnetite nanoparticles were synthesized and coated with silica for improved stability, followed by chitosan coating to enhance drug encapsulation and controlled release. Curcumin, a bioactive compound with neuroprotective properties, was loaded into the matrix of the magnetite nanoparticles. The physicochemical properties of the coated and uncoated nanoparticles were characterized using Fourier Transform Infrared Spectroscopy (FTIR), Scanning Electron Microscopy (SEM), Energy Dispersive Spectroscopy (EDS), and X-Ray Diffraction (XRD). Furthermore, drug release kinetics were analysed to compare the performance of the coated and uncoated magnetite nanoparticles.

2.0 Experimental Section

2.1 Materials

Glacial acetic acid (≥99%, Sigma-Aldrich) and ethanol (≥99.5%, Sigma-Aldrich) were used as solvents during bead preparation and silica functionalization. Sodium hydroxide (NaOH) pellets (BDH Chemicals) were used for neutralization and bead solidification, while hydrochloric acid (HCl, 7% v/v; Merck) was used during the demineralization stage of chitosan extraction.

Iron (III) chloride hexahydrate ($FeCl_3 \cdot 6H_2O$, ≥98%; Sigma-Aldrich) and iron(II) chloride tetrahydrate ($FeCl_2 \cdot 4H_2O$, ≥98%; Sigma-Aldrich) were used as precursors for magnetite nanoparticle synthesis. Tetraethyl orthosilicate (TEOS, 98%; Sigma-Aldrich) was used as the silica precursor for surface modification.

Curcumin powder (analytical grade; Loba Chemie) was used as the model drug for loading studies. Phosphate-buffered saline (PBS, pH 7.4) was used for in vitro release experiments. Double-distilled water was used throughout all preparation and washing procedures.

Crab shells were used as the source of chitin for chitosan extraction, and dried maize leaves were used in the green synthesis process.

2.2 Synthesis of Chitosan Using Crab Shell Waste

Chitosan was synthesized from crab shell waste via three sequential steps: demineralization, deproteination, and deacetylation, following the procedure of Aberoumand & Hoseinian (2025) .[20]

2.2.1 Demineralisation Phase

50 g of oven-dried crab shell powder (≤170 µm) was treated with 7 % v/v HCl (1:10 w/v) at room temperature under constant stirring for 2 hours to remove calcium carbonate. The mixture was filtered and washed repeatedly with distilled water to neutral pH, then dried at 60 °C for 24 hours.

2.2.2 Deproteination Phase

The demineralized shell powder was treated with 10 % w/v NaOH (1:10 w/v) at 90 °C for 2 hours to remove proteins. After filtration, the sample was washed until neutral pH, rinsed with ethanol, dried, ground, and sieved to ≤150 µm.

2.2.3 Deacetylation Phase

Chitin was converted to chitosan by treating 1 g of chitin with 15 mL of 40% w/w NaOH at 105 °C for 2 hours. The sample was filtered, washed to neutral pH, and dried at 60 °C. This step was repeated three times. Degree of deacetylation (DD) was determined by FTIR using the baseline method described by Szymańska & Winnicka (2015).[21]

2.3 Synthesis of Chitosan Beads Using Acetic Acid

Bead formation was done by dissolving 1 g of chitosan in 100 mL of 2% acetic acid. The resulting solution was added dropwise into 200 mL of 2 M NaOH (gelling medium) with constant stirring for 2 hours. Then after, the mixture was filtered and washed with distilled water to a pH of 7 (measured using a digital pH meter), then air-dried at room temperature (approximately 25 °C) for 8 hours.

2.4 Functionalization of Chitosan Beads Via SOL-GEL Process

A 2% TEOS solution was prepared using 2 mL TEOS, 6 mL 0.5 M HCl, and 92 mL distilled water. Two grams of chitosan were added to the TEOS solution and stirred using a magnetic stirrer (IKA® C-MAG HS 7) at 600 rpm until a uniform dispersion was obtained. The resulting beads were subsequently air-dried at ambient conditions (~25 ºC, no forced airflow) for 24 hours. The solution was aspirated and added dropwise into 300 mL of 2 M NaOH to form silica-coated chitosan beads following the method of Taufiq et al. (2020).[18] After 24 hours of continuous stirring at room temperature using a magnetic stirrer at 500 rpm, 50 mL of 2% acetic acid was added to stabilize the structure. The beads were filtered, washed to pH 7 and air-dried.

2.5 Preparation of the Maize Leaves Extract

Dried maize leaves (41.1 g) were ground into powder and mixed with 51 mL of distilled water. The mixture was filtered using a fine cotton cloth and Whatman No. 1 filter paper (110 mm diameter) to remove residual solids. The extract was stored at −4 °C to preserve its phytochemical stability and prevent microbial degradation prior to use in nanoparticle biosynthesis. This step was done once per synthesis batch and used across the replicates.

2.6 Synthesis of Magnetite Nanoparticles

$FeCl_3 \cdot 6H_2O$ (10.82 g) and $FeCl_2 \cdot 4H_2O$ (7.97 g) were dissolved in 200 mL distilled water and stirred for 20 minutes. Maize extract (40 mL) was added as a reducing agent. 2 M NaOH was added dropwise while monitoring pH to reach 11. A black precipitate of Fe_3O_4 formed and was collected with a magnet. The synthesis procedure was adapted from Paut et al. (2024).[12] The sample was washed and pH adjusted to 7, then dried at 100 °C.[13]

2.7 Synthesis of Chitosan Magnetite Nanoparticles

Four magnetite-to-chitosan ratios (25, 50, 75, and 100 wt%) were prepared by dissolving the corresponding amounts of magnetite nanoparticles in 12.5 mL of acetic acid, followed by sonication for 10 minutes to ensure uniform dispersion. Subsequently, 0.25 mL TEOS, 0.75 mL of 0.5 MHCl, and 11.5 mL of distilled water were added to each mixture. Chitosan (500 mg) was then introduced, except for the 100 wt% formulation, which served as the unloaded control. The resulting mixtures were stirred at room temperature for 30 minutes to obtain homogeneous suspensions before being added dropwise into 200 mL of 2 M NaOH. The formed beads were filtered, washed with distilled water until a neutral pH was achieved, and air-dried.

2.8 Calibration Curve

A 1 mg/mL (0.1% w/v) curcumin stock solution was prepared by dissolving 2 mg of curcumin in 2 mL of ethanol. To match the conditions of the in vitro release studies, serial dilutions (1–10 µg/mL) were subsequently prepared in a 50% v/v distilled water and 50% v/v ethanol mixture. The full UV-Vis spectrum (200–900 nm) of the solution was scanned, confirming a maximum absorbance (λ_{max}) at 430 nm. The absorbances of the serial dilutions were then measured at 430 nm to construct the calibration curve. The resulting regression

equation, whose graph is in Figure 1, was:

$$A = 0.19112C + 0.23234 \quad (1)$$

where A represents absorbance and C represents concentration (mg/µL). The regression coefficient obtained was $R^2 = 0.98131$.

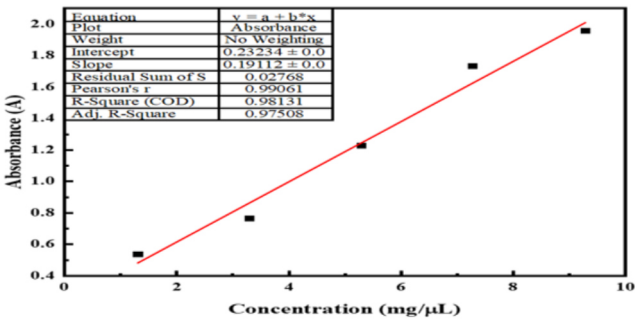

Figure 1. *Calibration curve of curcumin with maximum absorbance at 430 nm.*

for 10 minutes and vacuum treatment for 5 minutes. The final solution was stirred for 30 minutes until a homogeneous dispersion was obtained before dropwise addition into 2 M NaOH.

Loading was done using two different methods. In the first loading approach (Method 1) as shown in Figure 2, curcumin was incorporated during the formation of the chitosan–magnetite beads.

In the second loading approach (Method 2) as shown in Figure 3, curcumin was incorporated into pre-formed chitosan–magnetite beads using sonication. The solution was sonicated for 10 minutes using ultrasonic cleaner. The solution was introduced to a vacuum chamber for 5 minutes to remove all air content before adding NaOH before being washed and dried.

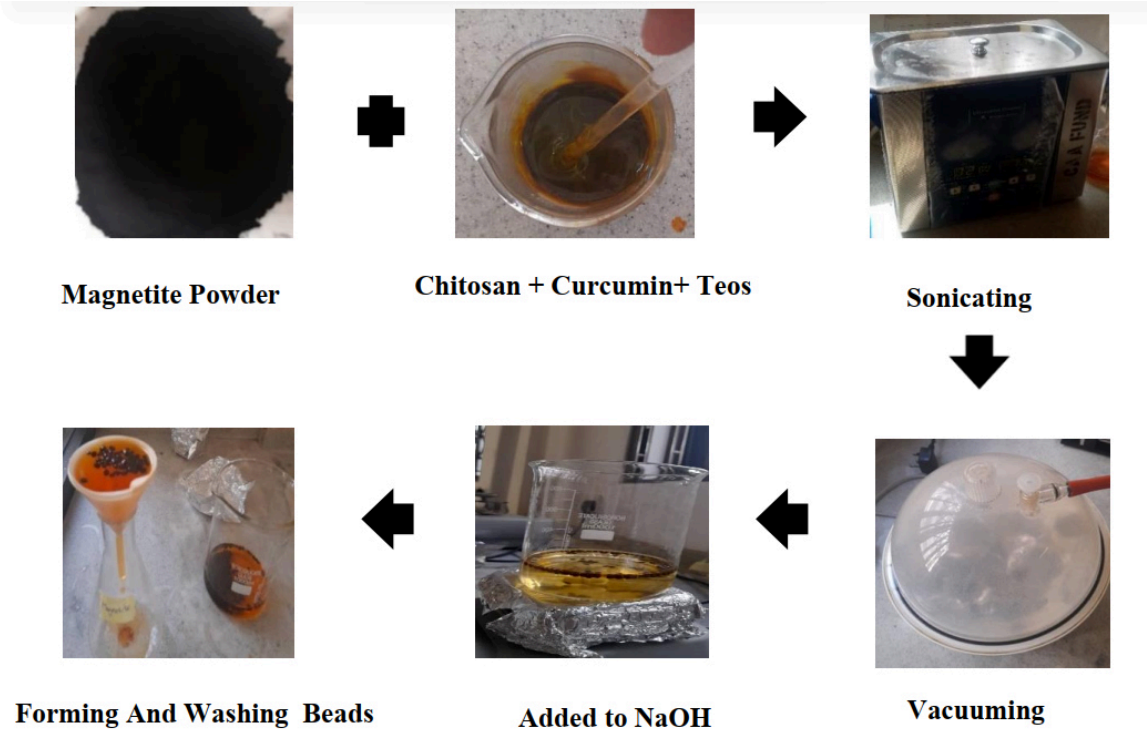

Figure 2. *Step-by-step experimental workflow for in situ drug loading via method 1*

2.9 Loading Magnetite – Chitosan Composite with Curcumin

To the chitosan-magnetite formulations (as described in Section 2.7), 1 mL of curcumin solution was added, followed by sonication

The resulting beads were obtained after stirring, dropwise addition into NaOH solution, followed by filtration, washing, and drying. This method achieved an entrapment efficiency of approximately 75%.

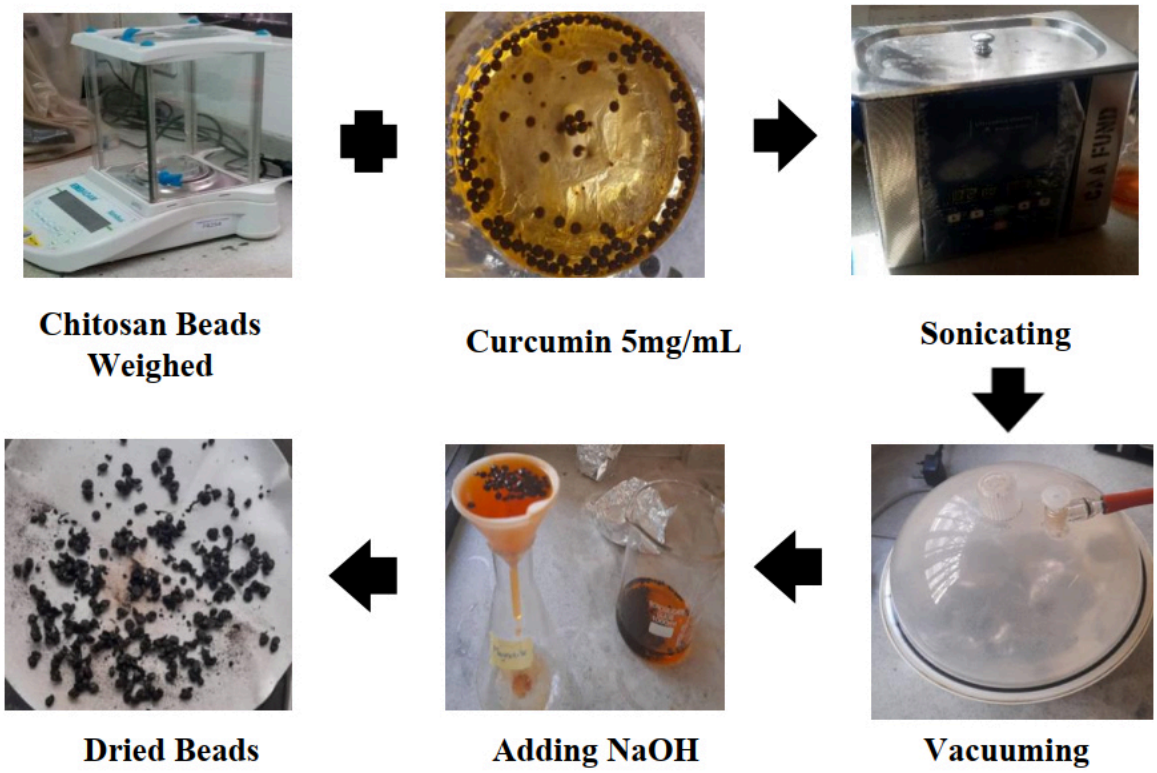

Figure 3. *Step-by-step experimental workflow for post synthesis drug loading via mehtod 2 (Post-Loading).*

2.10 Drug Releasing Study

20 mg of curcumin-loaded beads were added to 10 mL of PBS/alcohol (1:1 v/v) and the suspension was stirred continuously at 60 rpm for 24 hours at 37 °C throughout the release study. At 1-hour intervals, 3 mL aliquots were withdrawn and replaced with fresh medium.

2.11 Encapsulation Efficiency

10 mg of chitosan curcumin was weighed using a scale balance and added to 4 mL of ethanol. The resulting solution was vortexed and centrifuged. The yellowish supermatant was then collected and quantified using UV-Vis at 430 nm. Loading efficiency was then calculated from the relation in equation (2).

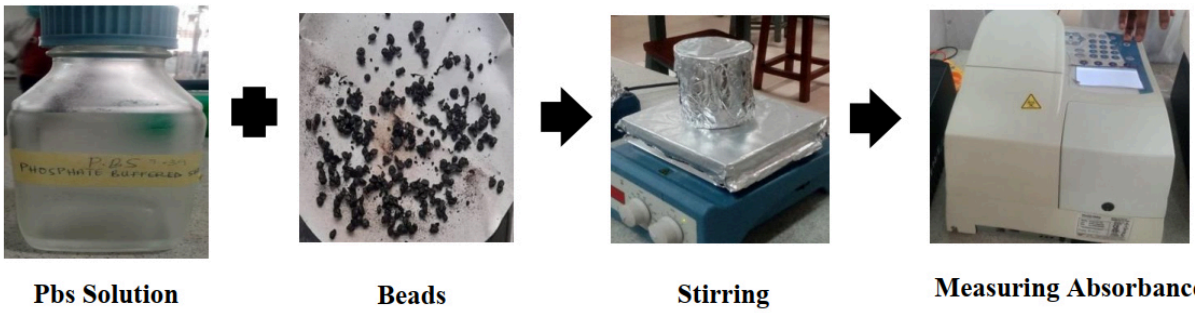

Figure 4. *Experimental workflow for the in vitro drug release kinetics study.*

Absorbance at 430 nm was measured to monitor cumulative drug release. The release profile of curcumin was monitored in PBS at pH 7.4 over the experimental period. Figure 4 summarizes this process.

$$Loading\ Efficiency = \frac{Total\ Amount\ of\ Curcumin\ Entrapped}{Total\ Amount\ of\ Curcumin\ Loaded} \times 100 \quad (2)$$

2.12 Physicochemical characterization

To confirm the successful synthesis and structural integrity of the coated and uncoated nanocomposites, the materials underwent a series of physicochemical characterizations.

As detailed in the following subsections, this multi-analytical approach brings together molecular, morphological, structural, and elemental evaluations to build a complete, well-rounded profile of the synthesized materials. The upcoming sections explore these findings by linking each method directly to its specific target: identifying functional groups via Fourier Transform Infrared Spectroscopy (FTIR), examining surface morphology and particle aggregation with Scanning Electron Microscopy (SEM), revealing crystallographic properties through X-ray Diffraction (XRD), and quantifying the elemental composition using Energy-Dispersive X-ray Spectroscopy (EDS).

2.12.1 Fourier- Transform Infrared spectroscopy (FTIR)

FTIR spectroscopy analysis was performed to identify and confirm the functional groups on surface of the synthetic materials (Chitosan and Magnetite) and to monitor their structural stability throughout the synthesis process. Specifically, this technique was used early on to determine the degree of deacetylation of the extracted chitin. As the synthesis progressed, it allowed the researchers to track characteristic absorption bands such as O–H and N–H stretching vibrations to detect enhanced intermolecular hydrogen bonding during bead formation.

2.12.2 Scanning Electron Microscopy (SEM)

The surface morphology of the synthesized nanoparticles and composites was examined using SEM (model: JEOL JSM-7610F). Prior to imaging, samples were air-dried and mounted on aluminium stubs using double-sided carbon tape. To enhance conductivity, samples were sputter-coated with a ~10 nm layer of gold using a Quorum SC7620 coater under an argon atmosphere (60 seconds at 20 mA). Imaging was conducted under high vacuum at an accelerating voltage of 5–15 kV, a working distance of ~10 mm, and a spot size of 3.0 µm. Images were captured at magnifications ranging from 500× to 50,000× to assess surface texture and particle aggregation.

2.12.3 Xray Diffraction (XRD)

While SEM provides valuable insights into the surface morphology and particle aggregation of the synthesized nanoparticles and composites, XRD was subsequently performed to analyse their underlying crystallographic properties. Specifically, XRD was utilized as a method to confirm the crystalline spinel cubic structure of the biosynthesized magnetite nanoparticles and to characterize the broad diffraction features indicative of chitosan's semi-crystalline, amorphous polymeric structure.

2.12.4 Energy-Dispersive Spectroscopy (EDS)

EDS analysis was performed to determine the elemental composition of the synthesized materials. The analysis was conducted under standard operating conditions at an accelerating voltage of 15 kV, with a spot size of approximately 1 µm and a live time of 60 s. For each sample, spectra were collected from five different regions (Spectrum 1–5), as indicated on the corresponding SEM micrographs in the results section, to ensure representative compositional analysis and minimize local heterogeneity.

3.0 Results

3.1 Fourier- Transform Infrared Spectroscopy (FTIR)

The FTIR spectra of raw chitosan, chitosan beads, and the chitosan–magnetite–curcumin composite are presented in transmittance mode, where absorption features appear as downward troughs. Band positions were identified based on the minima of these troughs. The FTIR spectrum of raw chitosan

(Figure 5a) shows a broad band around 3300–3400 cm^{-1}, a band near 1655 cm^{-1}, and additional bands in the region of 1378 and 1018 cm^{-1}. The FTIR spectrum of the chitosan–magnetite–curcumin composite (Figure 5b) also shows a broad band around 3308 cm^{-1}, with additional bands observed near 1557 cm^{-1}, 1034 cm^{-1}, and 416 cm^{-1}. The FTIR spectrum of chitosan beads (Figure 5c) retains the broad band around 3300–3400 cm^{-1}, with slight shifts and broadening. Additional bands are observed near 1642 cm^{-1} and 1022 cm^{-1}.

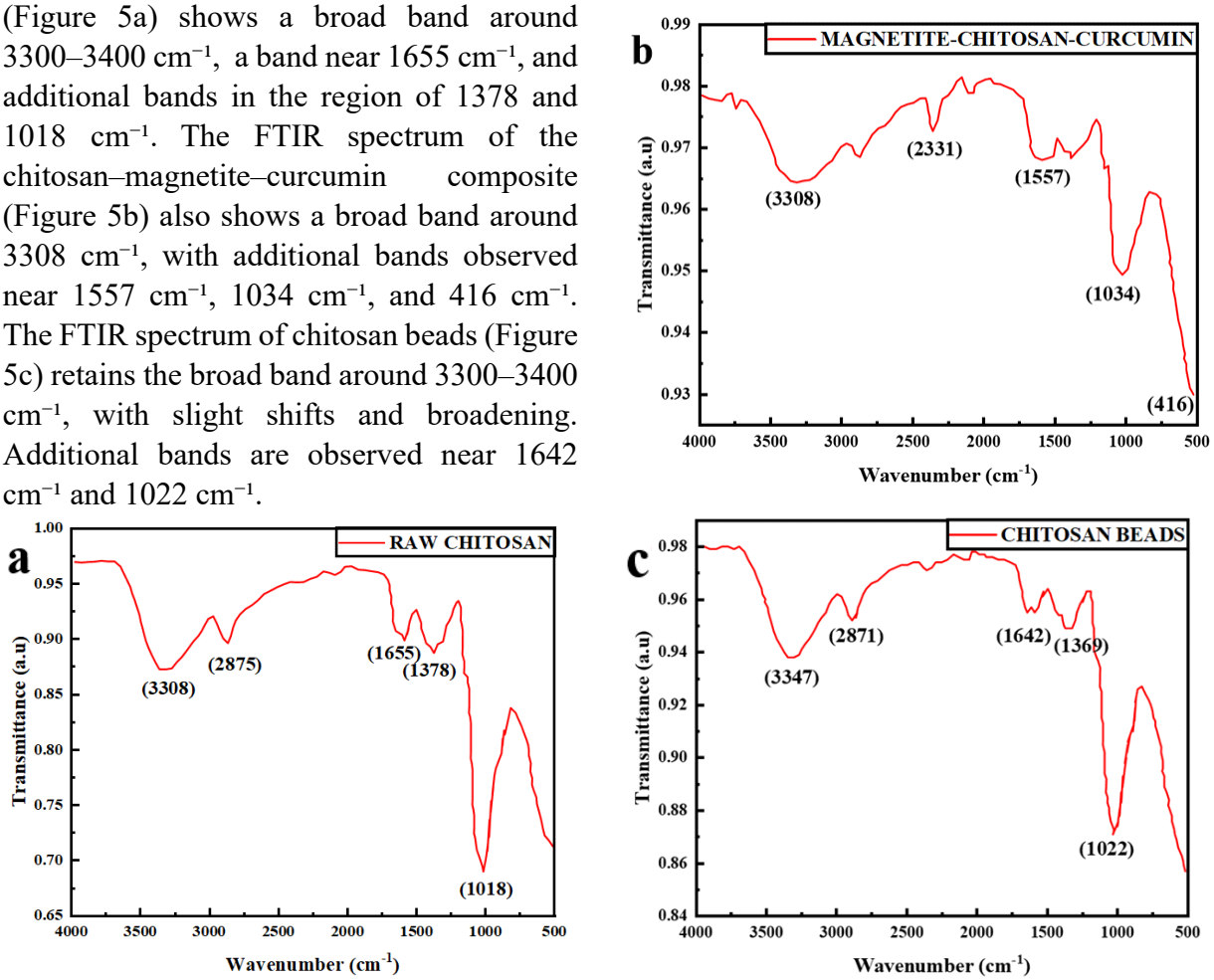

Figure 5. *FTIR Spectrum of a) Raw Chitosan, b) Magnetite Chitosan-Curcumin, and c) Chitosan Beads.*

3.2 Scanning Electron Microscopy (SEM)

The surface morphology of the samples was examined using scanning electron microscopy (SEM), as shown in Figure 6. Figure 6a displays the chitosan beads, which exhibit a rough and porous surface with visible irregularities. Figure 6b shows a heterogeneous surface characterized by irregular and less uniform structural features. The bare Fe_3O_4 nanoparticles (Figure 6c) consist of predominantly spherical particles with noticeable aggregation. For the polymer-coated Fe_3O_4 (Figure 6d), the micrographs reveal particles with a layered surface coating and reduced visibility of the underlying core structure. Finally, the curcumin sample (Figure 6e) presents elongated crystalline particles with well-defined edges and a compact morphology.

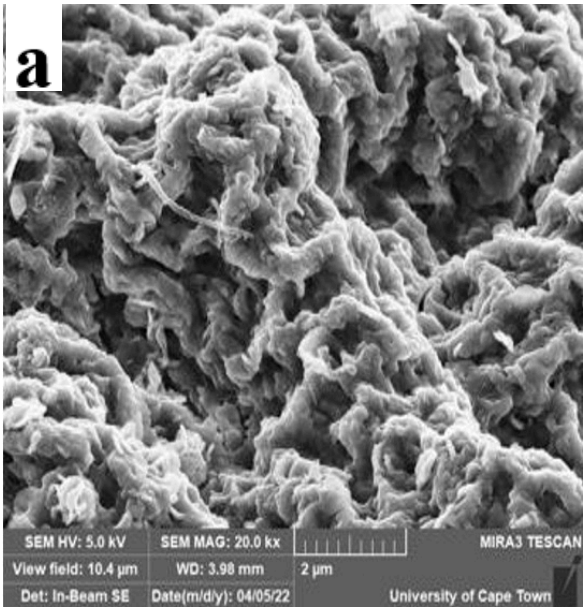

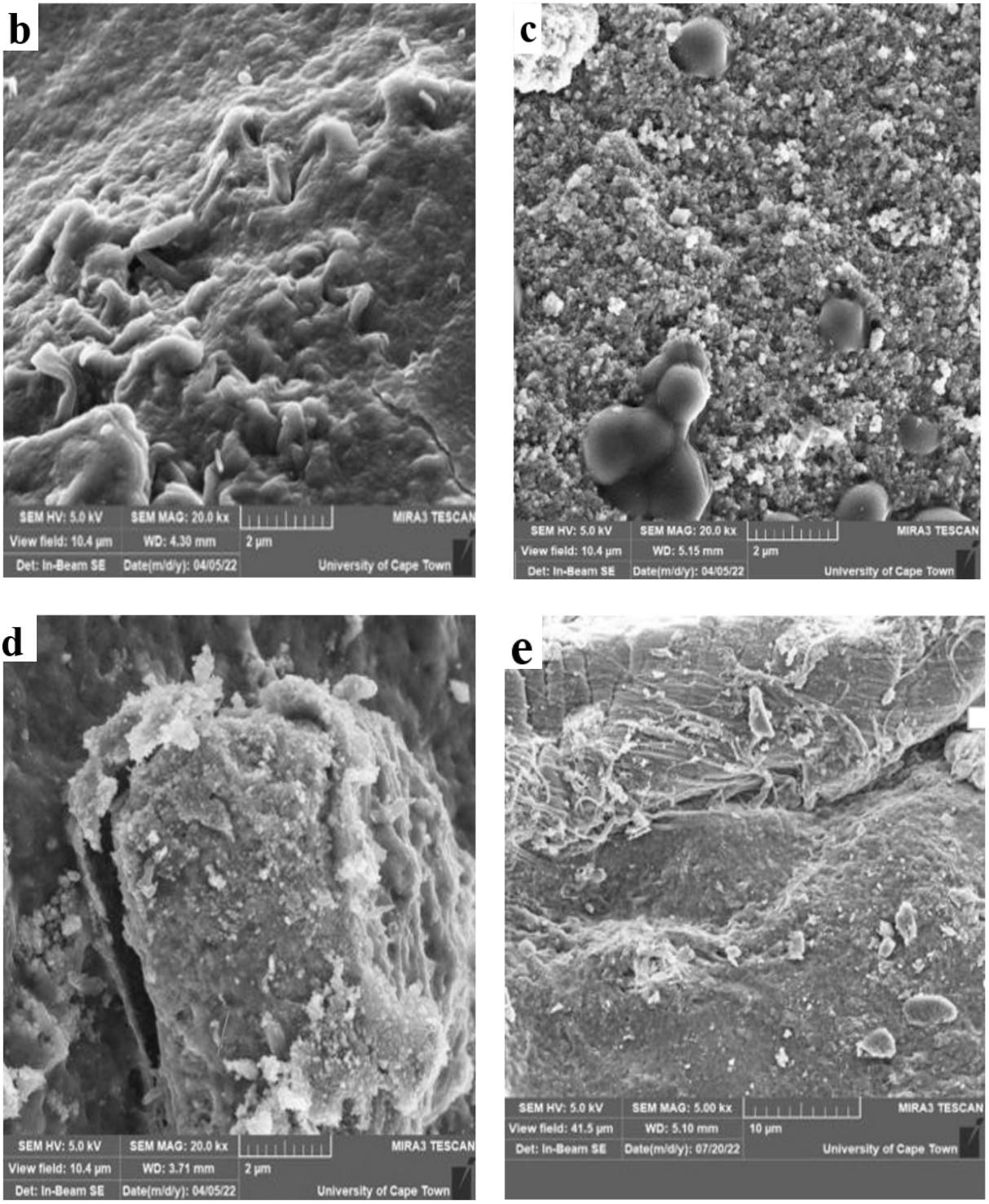

Figure 6. *SEM images showing (a) chitosan beads with porous morphology, (b) functionalized chitosan, (c) spherical magnetite nanoparticles, (d) polymer-coated magnetite, and (e) crystalline curcumin particles.*

3.3 X-Ray Diffraction (XRD)

Figure 7a shows a broad diffraction feature characteristic of semi-crystalline chitosan, indicating an amorphous polymeric structure. Figure 7b shows diffraction peaks at 2θ values of 10.0°, 20.0°, 44.0°, 65.0°, and 78.0°, corresponding to the (220), (311), (400), (422), and (511) crystallographic planes, respectively.

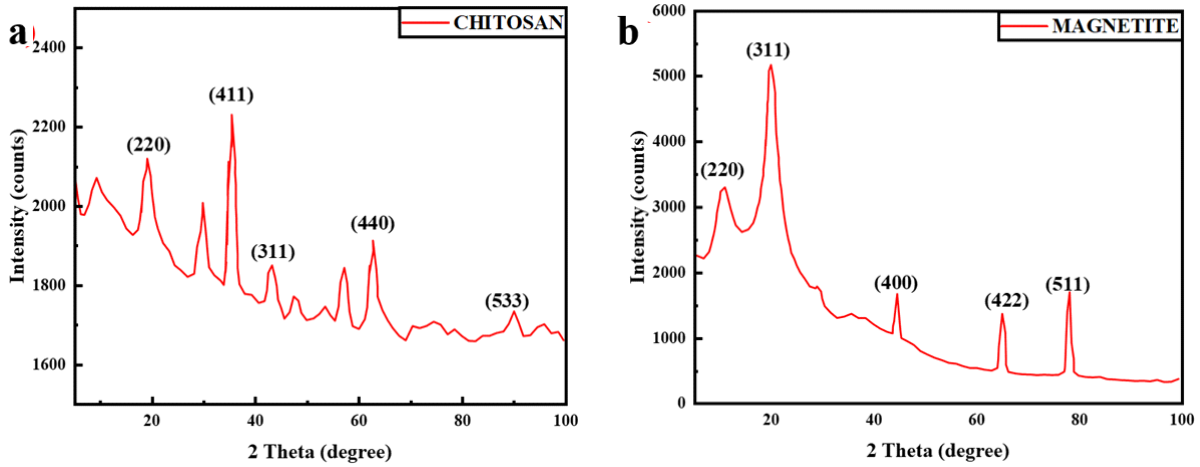

Figure 7. *Show the XRD pattern of (a) chitosan, (b) magnetite nanoparticles.*

The average crystallite size of the synthesized magnetite nanoparticles was calculated to be approximately 13 nm using the Debye–Scherrer equation:

$$D = \frac{K\lambda}{(\beta \cos \theta)} \quad (3)$$

where D is crystallite size, K is the shape factor (0.9), λ is the X-ray wavelength (0.15406 nm for Cu Kα), β is full width at half maximum, and θ is the Bragg angle. The crystallite size was calculated using the most intense (311) diffraction peak at 2θ = 20°, corresponding to a Bragg angle (θ) of 10°, with a full width at half maximum (FWHM, β) of 0.62° (converted to radians prior to calculation).

3.4 Energy Dispersive Spectroscopy (EDS)

In all EDS spectra, the x-axis represents X-ray energy (keV), while the y-axis represents X-ray intensity (counts per second per electron volt, cps/eV). The spectra are presented primarily for qualitative identification of elemental peaks, while quantitative elemental compositions were obtained directly from the EDS software through peak integration and averaging across the sampled regions (n = 5).

3.4.1 Chitosan Beads

Figure 8 shows the EDS spectrum of the chitosan beads, acquired from the selected regions indicated in the SEM image. The spectrum exhibits dominant peaks corresponding to carbon (C) and oxygen (O), which are characteristic of the chitosan polymer backbone. The quantitative elemental composition, obtained by averaging across the five sampled regions, is presented in Table 1.

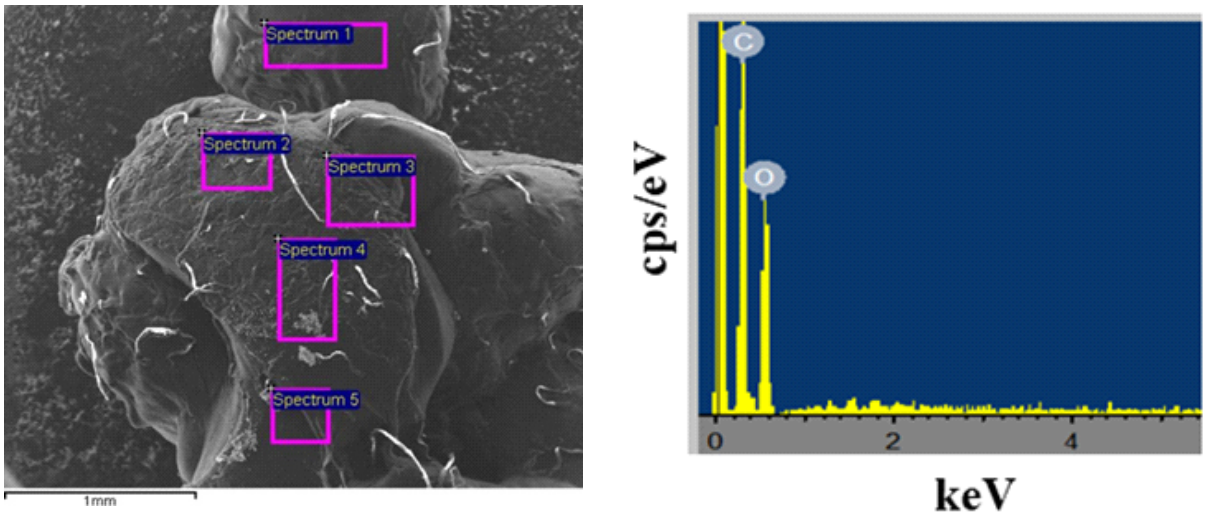

Figure 8. *EDS spectrum of chitosan beads showing the 5 sample spectrums on the left and the elemental composition (Carbon and Oxygen) on the right.*

Table 1. *Summary of Elemental Composition of Chitosan Beads Based on EDS Analysis (N = 5).*

Element	Mean Composition (at.%) ± SD
Oxygen	50.38 ± 1.50
Carbon	49.62 ± 1.50

The chitosan beads consist primarily of oxygen (50.38 ± 1.50 at.%) and carbon (49.62 ± 1.50 at.%), confirming the organic nature of the material. These findings are consistent with previously reported compositions of chitosan-based systems.

3.4.2 Chitosan Magnetite Composite 50 wt%

The EDS spectrum of the chitosan–magnetite composite (50 wt%) is presented in Figure 9.

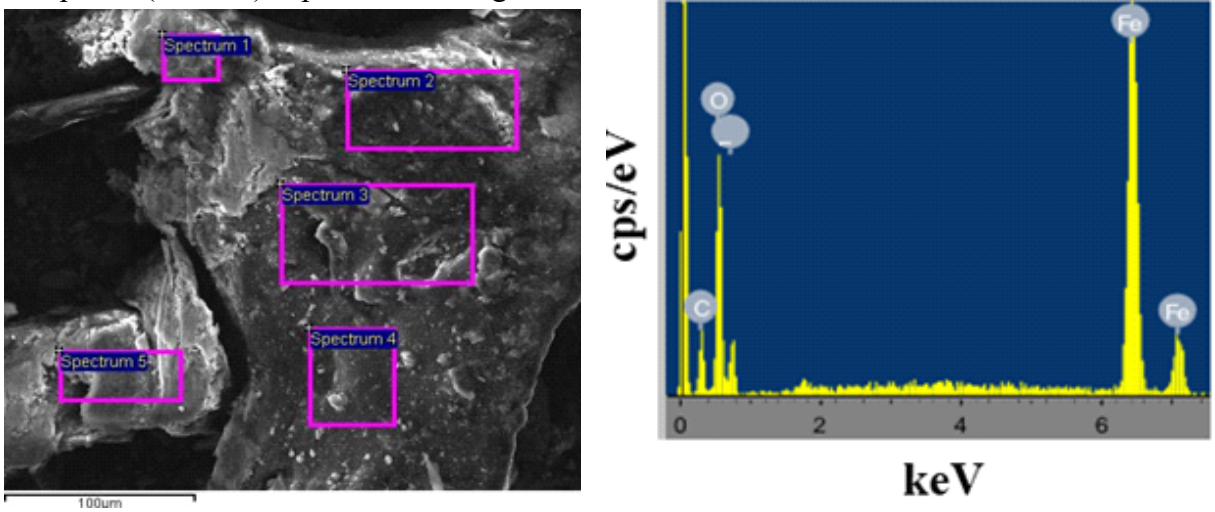

Figure 9. *EDS Spectrum of Chitosan–Magnetite Composite (50 wt%) showing the 5 sample spectrums on the left and the elemental composition (Carbon, Oxygen and Iron) on the right.*

Table 2. *Summary of Elemental Composition of Chitosan–Magnetite Composite (50 wt%) Based on EDS Analysis (N = 5).*

Element	Mean Composition (at.%) ± SD
Oxygen	35.58 ± 10.70
Carbon	37.25 ± 9.15
Iron	27.17 ± 15.14

In addition to the characteristic carbon and oxygen peaks, a distinct iron (Fe) peak is observed. Quantitative analysis of the spectra, averaged over five sampled regions, is summarized in Table 2. The composition includes oxygen (35.58 ± 10.70 at.%), carbon (37.25 ± 9.15 at.%), and iron (27.17 ± 15.14 at.%).

3.4.3 Chitosan–Silica Beads

Figure 10 shows the EDS spectrum of the chitosan–silica beads. The spectrum reveals prominent peaks corresponding to oxygen (O), carbon (C), and silicon (Si). Minor peaks corresponding to magnesium (Mg) and calcium (Ca) are also observed. The averaged elemental composition (n = 5) is presented in Table 3, showing oxygen (59.08 ± 3.24 at.%), carbon (29.45 ± 6.32 at.%), silicon (4.07 ± 1.76 at.%), magnesium (3.97 ± 1.88 at.%), and calcium (3.02 ± 4.59 at.%). The presence of silicon confirms successful silica functionalization, while the overall elemental distribution supports the formation of a hybrid organic–inorganic composite system.

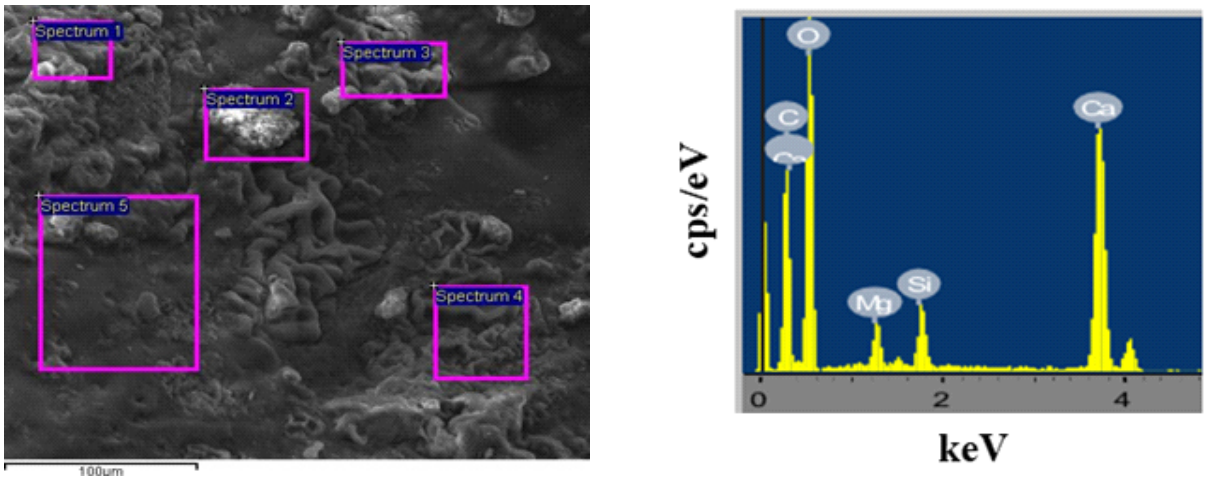

Figure 10. *EDS spectrm of chitosan-silica beads showing the 5 sample spectrums on the left and the elemental composition (Carbon, Oxygen,* Magnesium, Silicon, Calcium*) on the right.*

Table 3. *Summary of Elemental Composition of Chitosan–Silica Beads Based on EDS Analysis (N = 5).*

Element	Mean Composition (at.%) ± SD
Oxygen	59.08 ± 3.24
Carbon	29.45 ± 6.32
Magnesium	3.97 ± 1.88
Silicon	4.07 ± 1.76
Calcium	3.02 ±4.59

3.5 Entrapped Efficiency

Method 1 consistently demonstrated superior performance across the evaluation spectrum because the active compound was fully incorporated during the initial phase of bead formation. This co-formulation approach allowed the cross-linking polymer network to develop directly around the drug molecules, capturing them deeply within the evolving chitosan–magnetite structural matrix for a more robust encapsulation. This synchronous assembly process maximizes spatial distribution within the inner core of the sphere while minimizing premature surface migration of the compound. Conversely Method 2 yielded lower overall performance trends. Because the architectural matrix of the beads was already completely cross-linked prior to drug exposure, subsequent penetration into the tight, preformed polymeric network remained highly constrained. The dense outermost boundary layer essentially acted as a physical barrier to diffusion, preventing deep core loading. Consequently, the adsorption was confined primarily to superficial adsorption, even though targeted ultrasonic processing successfully enhanced baseline surface dispersion (see Figure 11).

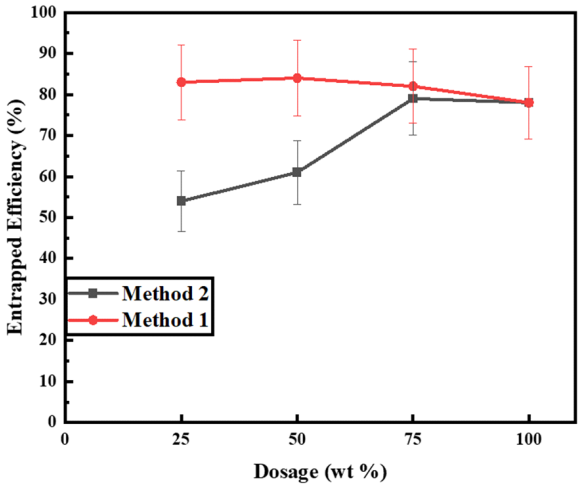

Figure 11. *Quantitative comparison of curcumin entrapment efficiency between method 1 and method 2 processing pathways.*

3.6 Cumulative Drug Release Profile

The observed CRP release profiles demonstrated a clear dependence on initial loading concentrations over a monitored

15-hour duration (see Figure 12). The 100% CRP formulation stands out distinctly, exhibiting a rapid initial burst effect that peaks sharply at 2 hours before steadily decaying over the remaining time domain. In stark contrast, the 75%, 50%, and 25% CRP formulations exhibit a highly synchronized, overlapping baseline trajectory during the first 7 hours, indicating uniform diffusion resistance across these lower loading concentrations. A notable anomaly occurs exclusively within the 25% CRP profile, which undergoes a prominent, transient acceleration between Hour 7 and Hour 8. This localized spike, peaking distinctly at the 8-hour mark, suggests a sudden, temporary structural relaxation or localized fracturing within the polymer network that briefly opened enhanced macro-porous diffusion pathways. Following this sudden release event, the 25% profile decays rapidly, rejoining the stable, clustered baseline maintained by the 50% and 75% formulations from Hour 10 through the end of the study.

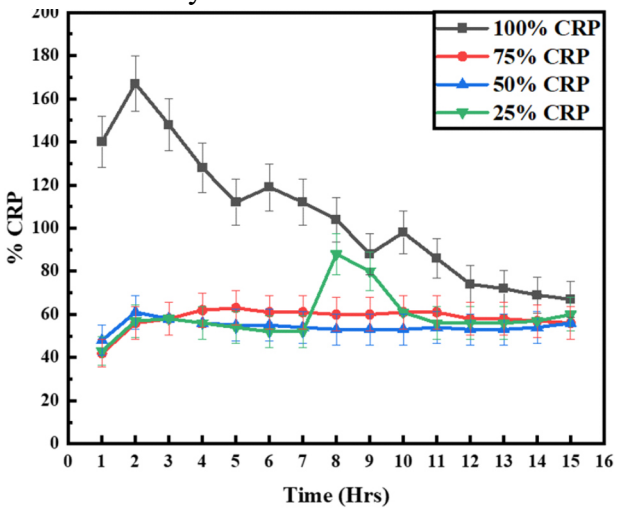

Figure 12. *Graph showing the Drug Release Profile of different CPR formulations over a 15 hour period.*

4.0 Discussion

4.1 Fourier- Transform Infrared Spectroscopy (FTIR) Results

In the FTIR spectrum of chitosan beads (Figure 5c), the broad O–H/N–H stretching band is retained but appears slightly shifted and broadened, suggesting enhanced intermolecular hydrogen bonding following bead formation and hydration. Similar effects of ionic gelation and bead formation on chitosan FTIR spectra have been reported by Szymańska and Winnicka.[20] Minor features observed in the near-infrared region are weak and may be influenced by environmental CO_2 or residual moisture; therefore, no strong structural assignments are made for these bands.

The FTIR spectrum of the chitosan–magnetite–curcumin composite (Figure 5b) preserves the characteristic absorption bands of chitosan, indicating that the polymer backbone remains intact after composite formation.[9, 22] The observed spectral features and band shifts support the successful formation of the composite system while maintaining the structural integrity of chitosan, in agreement with previously reported chitosan–magnetite-based materials.[22]

4.2 Scanning Electron Microscopy (SEM)

The surface morphology of the synthesized nanoparticles and composites was examined using scanning electron microscopy (SEM) (JEOL JSM-7610F). Prior to imaging, samples were air-dried and mounted on aluminium stubs using double-sided carbon tape. To enhance conductivity, samples were sputter-coated with a ~10 nm layer of gold using a Quorum SC7620 coater under an argon atmosphere (60 seconds at 20 mA). Imaging was conducted under high vacuum at an accelerating voltage of 5–15 kV, a working distance of ~10 mm, and a spot size of 3.0 µm. Images were captured at magnifications ranging from 500× to 50,000×.

The SEM image of chitosan beads (Figure 6a) reveals a rough and porous morphology, which is favourable for drug encapsulation. This observation is consistent with previous studies reporting similar porosity in chitosan-based carriers for enhanced drug retention and controlled release.[23]

The porous and rough morphology observed in chitosan beads (Figure 6a) is advantageous for drug loading due to the increased surface area and potential for drug entrapment within the porous network. Similar porous structures in chitosan-based systems have been reported to enhance encapsulation efficiency and controlled release behaviour in drug delivery applications. Figure 6b shows a visibly more heterogeneous and irregular surface morphology compared to the relatively uniform porous structure observed in Figure 6a. This observation is based on qualitative visual inspection of SEM micrographs rather than quantitative surface roughness measurements.[24] The more heterogeneous surface observed in Figure 6b suggests structural modification or variation in particle formation compared to the native chitosan matrix. Such irregularity may influence surface interaction and drug adsorption behaviour.

Figure 6c presents biosynthesized Fe_3O_4 nanoparticles exhibiting a spherical shape and uniform aggregation, consistent with characteristics of plant-mediated magnetic nanoparticles.[24] The spherical morphology and aggregation of Fe_3O_4 nanoparticles (Figure 6c) are typical of magnetite-based nanostructures, where magnetic dipole interactions often lead to cluster formation.

Figure 6d shows polymer-coated Fe_3O_4 particles with a visibly heterogeneous and layered surface, confirming chitosan deposition, as similarly observed in magnetite-polymer nanocomposites.[24] The polymer-coated Fe_3O_4 nanoparticles (Figure 6d) demonstrate surface layering consistent with successful coating of magnetite cores by a polymer matrix. This coating is known to improve stability and biocompatibility while modifying surface characteristics for functional applications in drug delivery systems. Figure 6e depicts the crystalline morphology of curcumin, with elongated particles as expected from prior morphological analyses.[23] The crystalline, elongated morphology of curcumin (Figure 6e) aligns with previously reported structural characteristics of curcumin in its native form, which is known to exhibit limited solubility due to its crystalline nature.

Overall, the SEM analysis confirms distinct morphological transitions across raw materials and composite formation, indicating successful fabrication of the nanoparticle system, although quantitative surface roughness and particle size distribution analyses were not performed.

4.3 X-Ray Diffraction (XRD)

The broad diffraction feature observed in chitosan (Figure 7a) indicates its semi-crystalline nature, which is typical of polysaccharide-based polymers due to disruption of ordered chain packing by hydrogen bonding.

The diffraction peaks observed in Figure 7b correspond to the (220), (311), (400), (422) and (511) planes, confirming the crystalline structure of magnetite nanoparticles. The peak positions are consistent with the standard JCPDS No. 19-0629, indicating formation of a cubic spinel Fe_3O_4 phase.[25]

The calculated crystallite size of approximately 13 nm suggests the formation of nanoscale magnetite particles, which is consistent with the expected size range for biosynthesized magnetic nanoparticles. Such nanoscale dimensions are important for enhancing surface area and magnetic responsiveness in drug delivery applications.

4.4 Energy Dispersive Spectroscopy (EDS)

The EDS analysis confirms the elemental composition of the synthesized materials across all samples. The chitosan beads are

composed primarily of carbon and oxygen, which is consistent with the expected composition of polysaccharide-based biopolymers. The chitosan–magnetite composite shows additional iron peaks, confirming successful incorporation of Fe_3O_4 nanoparticles into the chitosan matrix. The presence of iron, alongside carbon and oxygen, indicates successful formation of the composite structure.

The chitosan–silica beads exhibit additional silicon peaks, confirming successful silica functionalization. The presence of magnesium and calcium is attributed to residual mineral content from natural precursors used during synthesis.

Overall, the EDS results confirm successful formation of the different composite systems, with elemental distributions consistent with the intended material synthesis routes.

4.4.1 Chitosan Beads

The elemental composition of the chitosan beads confirms the dominance of carbon and oxygen, which is characteristic of chitosan's polysaccharide backbone. This composition reflects the organic nature of the material and the presence of hydroxyl and amino functional groups within the polymer structure. The absence of additional inorganic elements further supports the purity of the chitosan matrix and its successful extraction.

4.4.2 Chitosan Magnetite Composite 50 wt%

The presence of iron (Fe) in the EDS spectrum confirms the successful incorporation of magnetite nanoparticles into the chitosan matrix. The coexistence of carbon, oxygen, and iron indicates the formation of a hybrid organic–inorganic composite. The distribution of these elements suggests effective integration of Fe_3O_4 within the polymeric network, which is essential for imparting magnetic functionality to the system. The relatively high standard deviations in elemental composition further suggest heterogeneous dispersion of magnetite within the chitosan matrix, which is typical in polymer–nanoparticle composites.

4.4.3 Chitosan–Silica Beads

The detection of silicon (Si) confirms successful incorporation of silica into the chitosan structure, indicating successful functionalization of the polymer matrix. The presence of oxygen and carbon alongside silicon reflects the hybrid organic–inorganic nature of the composite. Additionally, the detection of magnesium and calcium is attributed to residual mineral components originating from the natural crab shell precursor, which is commonly reported in biologically derived chitosan systems. These trace elements do not interfere with the primary composite formation but indicate the natural origin of the starting material.

4.5 In Vitro Release Studies

The release of curcumin from the silica-containing magnetite system in physiological pH (7.4) is influenced by interactions between silanol and hydroxyl groups present on the silica surface. At pH 7.4, these functional groups interact with the surface of the magnetite nanoparticles, leading to partial pore blockage, which reduces diffusion pathways for the encapsulated drug. This results in a slower release rate of curcumin from the nanoparticle system.[26]

This controlled release behaviour indicates that the silica matrix plays a significant role in regulating drug diffusion under physiological conditions, supporting its potential application in sustained drug delivery systems.

4.6 Entrapped Efficiency

The contrasting encapsulation outcomes between the two processing pathways reveal

critical insights into the mass-transfer and cross-linking kinetics of the system. The significantly higher entrapment efficiency consistently observed in Method 1 is directly attributed to the synchronous assembly of the structural matrix. By introducing curcumin into the bulk polymer solution prior to droplet extrusion, the cross-linking network of the chitosan-magnetite matrix forms in situ around the heavily dispersed drug molecules. This simultaneous gelation traps the compound deeply within the core architecture, preventing significant molecular migration and structural leakage into the external alkaline bath.

In contrast, the marked reduction in entrapment efficiency characteristic of Method 2 highlights the physical limitations of a post-loading strategy on a fully cross-linked system. When preformed, solidified chitosan-magnetite beads are immersed in a secondary drug solution, the dense, pre-existing polymeric network acts as a strict steric barrier to internal diffusion. Even though targeted sonication successfully maximizes external dispersion and overcomes superficial boundary-layer resistance, it is structurally incapable of driving the hydrophobic curcumin molecules past the cross-linked outermost shell into the compact core of the bead. Consequently, retention remains largely confined to weak surface adsorption, which is highly prone to rapid leakage during processing. The clear technical superiority of the co-formulation mechanism in Method 1 thus provides the foundational rationale for its selection in subsequent controlled drug release optimization studies.

4.7 Cumulative Drug Release Profile

The observed CRP release kinetics (see Figure 12) demonstrate a complex, concentration-dependent relationship that departs from idealized swelling models. The rapid initial release observed exclusively in the 100 wt% formulation is indicative of a classic burst release effect. This phenomenon is typically driven by high thermodynamic drug activity at maximum loading capacity, forcing loosely bound, surface-associated molecules to diffuse rapidly into the surrounding medium. Conversely, the 75 wt% and 50 wt% formulations exhibit highly clustered, suppressed release trajectories throughout the entire 15-hour window. This prolonged, overlapping deceleration points to strong intermolecular interactions, such as extensive hydrogen bonding, between the compound and the dense chitosan–magnetite network, which significantly increases structural resistance to mass transfer and forces a highly controlled, matrix-degradation release behavior.[27]

The most striking anomalous behavior occurs within the lower-loaded 25 wt% formulation. Rather than sustaining the slowest overall release profile as might be expected in traditional homogeneous matrices, this system follows the restricted baseline cluster until undergoing a sharp, localized release acceleration precisely between Hour 7 and Hour 8. This prominent peak at the 8-hour mark contradicts standard single-phase diffusion theories; instead, it indicates a distinct structural transition within the hydrogel network. This transient spike is heavily indicative of macromolecular chain relaxation, matrix erosion, or localized micro-fracturing of the preformed shell, which temporarily opens high-permeability structural pathways before the system stabilizes and decays back to the baseline profile by Hour 10. This multi-phase delivery pattern emphasizes that in low-concentration frugal polymer matrices, release pathways are heavily dictated by dynamic structural transitions within the cross-linked network rather than simple concentration gradients alone.[28]

Overall, moderate drug loading levels (50 wt% and 75 wt%) provide a more balanced release profile, combining reduced burst release with sustained drug delivery. These

formulations are therefore more suitable for controlled drug delivery applications, including cancer therapy, where prolonged and regulated release is desirable.

5.0 Conclusion

This study successfully developed a low-cost, eco-friendly drug delivery system using chitosan-magnetite nanoparticles coated with silica for targeted and sustained release of curcumin. Chitosan was synthesized from crab shell waste, while magnetite nanoparticles were biosynthesized using maize leaf extract and coated via the sol–gel method.

Structural analysis using XRD and FTIR confirmed successful synthesis of the nanocomposite, and in vitro drug release studies demonstrated controlled, sustained release behaviour particularly in the 75 wt% formulation, which showed the highest entrapment efficiency. These findings highlight the potential of silica-coated chitosan-magnetite nanoparticles as an effective, biocompatible vehicle for drug delivery. The simplicity, use of natural waste materials, and affordability make this system especially promising for cancer treatment in low- and middle-income countries (LMICs), where access to advanced therapies is limited.

Future studies should involve in vivo evaluations in animal models to assess biodistribution, toxicity, and therapeutic efficacy in biological systems. Although curcumin was used as a model drug, the dual-coated nanoparticle system may be adapted for both hydrophilic and hydrophobic drugs, expanding its applicability to other chemotherapeutics and neuroprotective agents. Despite promising in vitro results, translation into LMIC settings requires careful consideration of regulatory barriers, local manufacturing capacity, and distribution logistics. Collaborations with local health agencies and the development of scalable synthesis protocols will be crucial for real-world implementation.

Authors' Contributions

The project was conceptualized collaboratively by all contributors. JAN served as the principal author, conducted the experiments, and prepared the initial draft of the manuscript. JG contributed to manuscript refinement. HA and PEA, along with RA provided supervisory oversight, helped refine the research objectives, and critically reviewed the manuscript for intellectual content. All authors read and approved the final version of the manuscript.

Declaration of Interests

The authors declare that they have no known competing financial interests or personal relationships that could have appeared to influence the work reported in this paper.

References

1. Ferlay J, Colombet M, Soerjomataram I, Parkin DM, Pineros M, Znaor A, et al. Cancer statistics for the year 2020: An overview. Int J Cancer. 2021.

2. World Health Organization 2020. World Health Statistics 2020.

3. Sung H, Ferlay J, Siegel RL, Laversanne M, Soerjomataram I, Jemal A, et al. Global Cancer Statistics 2020: GLOBOCAN Estimates of Incidence and Mortality Worldwide for 36 Cancers in 185 Countries. CA Cancer J Clin. 2021;71(3):209-49.

4. Pramesh CS, Badwe RA, Bhoo-Pathy N, Booth CM, Chinnaswamy G, Dare AJ, et al. Priorities for cancer research in low- and middle-income countries: a global perspective. Nature Medicine. 2022;28(4):649-57.

5. Basu P, Lucas E, Zhang L, Muwonge R, Murillo R, Nessa A. Leveraging vertical COVID-19 investments to improve monitoring of cancer screening programme - A case study from Bangladesh. Prev Med. 2021;151:106624.

6. Singh R, Kumar CS, Banerjee M, Gupta S. Correction to A Dual Drug Delivery Platform for Cancer-Bacteria Cotargeting. ACS Appl Bio Mater. 2020;3(3):1827.

7. Rinaudo M. Chitin and chitosan: Properties and applications. Progress in Polymer Science. 2006;31(7):603-32.

8. Medina-Moreno A, El-Hammadi MM, Martínez-Soler GI, Ramos JG, García-García G, Arias JL. Magnetic and pH-responsive magnetite/chitosan (core/shell) nanoparticles for dual-targeted methotrexate delivery in cancer therapy. Drug Delivery and Translational Research. 2025;15(5):1646-59.

9. Fathi R, Mohammadi R. Preparation of pH-responsive magnetic nanocomposite hydrogels based on k-carrageenan/chitosan/silver nanoparticles: Antibacterial carrier for potential targeted anticancer drug delivery. Int J Biol Macromol. 2023;246:125546.

10. Prabaharan M. Chitosan-based nanoparticles for tumor-targeted drug delivery. Int J Biol Macromol. 2015;72:1313-22.

11. Topić Popović N, Lorencin V, Strunjak-Perović I, Čož-Rakovac R. Shell Waste Management and Utilization: Mitigating Organic Pollution and Enhancing Sustainability. Applied Sciences. 2023;13(1):623.

12. Paut A, Guć L, Vrankić M, Crnčević D, Šenjug P, Pajić D, et al. Plant-Mediated Synthesis of Magnetite Nanoparticles with Matricaria chamomilla Aqueous Extract. Nanomaterials. 2024;14(8):729.

13. Kiwumulo HF, Muwonge H, Ibingira C, Lubwama M, Kirabira JB, Ssekitoleko RT. Green synthesis and characterization of iron-oxide nanoparticles using Moringa oleifera: a potential protocol for use in low and middle income countries. BMC Res Notes 15, 149 (2022). https://doi.org/10.1186/s13104-022-06039-7

14. Christian P, Von der Kammer F, Baalousha M, Hofmann T. Nanoparticles: structure, properties, preparation and behaviour in environmental media. Ecotoxicology. 2008;17(5):326-43.

15. Mbabazize GM, Kagisha V, Njunwa KJ, Oloro J. The effect of prescription patterns on the performance of the pharmacy department of a Regional Referral Hospital, Uganda. Journal of Pharmaceutical Policy and Practice. 2024;17(1):2306852.

16. De Beus A, Fabry T, Lacker H. A gastric acid secretion model. Biophysical journal. 1993;65(1):362-78.

17. Dhavale RP, Dhavale RP, Sahoo SC, Kollu P, Jadhav SU, Patil PS, et al. Chitosan coated magnetic nanoparticles as carriers of anticancer drug Telmisartan: pH-responsive controlled drug release and cytotoxicity studies. Journal of Physics and Chemistry of Solids. 2021;148.

18. Taufiq A, Nikmah A, Hidayat A, Sunaryono S, Mufti N, Hidayat N, et al. Synthesis of magnetite/silica nanocomposites from natural sand to create a drug delivery vehicle. Heliyon. 2020;6(4):e03784.

19. Harkins AL, Duri S, Kloth LC, Tran CD. Chitosan–cellulose composite for wound

dressing material. Part 2. Antimicrobial activity, blood absorption ability, and biocompatibility. Journal of Biomedical Materials Research Part B: Applied Biomaterials. 2014;102(6):1199-206.

20. Aberoumand A, Hoseinian M. Extraction of Chitosan from shells of crab (Liocarcinus vernalis). Applied Food Research. 2025;5(1):100964.

21. Szymańska E, Winnicka K. Stability of Chitosan—A Challenge for Pharmaceutical and Biomedical Applications. Marine Drugs. 2015;13(4):1819-46.

22. Li J, Cai C, Li J, Li J, Li J, Sun T, et al. Chitosan-Based Nanomaterials for Drug Delivery. Molecules. 2018;23(10).2661.

23. Mitra A, Dey B. Chitosan microspheres in novel drug delivery systems. Indian journal of pharmaceutical sciences. 2011;73(4):355.

24. Das AK, Marwal A, Pareek V, Joshi Y, Apoorva A. Surface Engineering of Magnetite Nanoparticles by Plant Protein: Investigation into Magnetic Properties. Nano Hybrids and Composites. 2016;11:38-44.

25. Shameli K, Ahmad MB, Zamanian A, Sangpour P, Shabanzadeh P, Abdollahi Y, et al. Green biosynthesis of silver nanoparticles using Curcuma longa tuber powder. International journal of nanomedicine. 2012:5603-10.

26. Kazemzadeh P, Sayadi K, Toolabi A, Sayadi J, Zeraati M, Chauhan NPS, et al. Structure-Property Relationship for Different Mesoporous Silica Nanoparticles and its Drug Delivery Applications: A Review. Front Chem. 2022;10:823785.

27. Peppas NA, Sahlin JJ. A simple equation for the description of solute release. III. Coupling of diffusion and relaxation. International journal of pharmaceutics. 1989;57(2):169-72.

28. Garg U, Chauhan S, Nagaich U, Jain N. Current Advances in Chitosan Nanoparticles Based Drug Delivery and Targeting. Adv Pharm Bull. 2019;9(2):195-204.